arXiv:astro-ph/0108096v1 6 Aug 2001

A 12–DAY *ASCA* OBSERVATION OF THE NARROW-LINE SEYFERT 1 GALAXY TON S180: TIME-SELECTED SPECTROSCOPY

P. ROMANO[1], T.J. TURNER[2,3], S. MATHUR[1], & I.M. GEORGE[2,3]

ABSTRACT

We present an analysis of the X-ray variability properties of the narrow-line Seyfert 1 galaxy Ton S180, based upon a 12-day continuous observation with *ASCA*. Examination of the light curves reveals flux variations of a factor of 3.5 in the 0.7–1.3 keV band and 3.9 in the 2–10 keV band. Time-resolved spectroscopy, using approximately daily sampling, reveals that the broad "soft hump" component at energies < 2 keV shows flux variations on timescales as short as 1 day that are well correlated with the photon index and the 2–10 keV band flux. A broad Fe Kα emission is detected. There is also a statistically significant evidence for a narrow Fe Kα line at ~ 6.8 keV, indicating an origin in ionized material. We do not detect significant variations of the Fe Kα line flux or equivalent width on timescales of ~ 1 day–1 week.

Despite evidence for correlated events in the power-law and soft hump on timescales of a day, the flux correlations clearly do not exist on all timescales. In particular, the softness ratio reveals spectral variability on timescales as short as ~ 1000 s, indicating that the power-law continuum and soft hump fluxes are not well correlated on this timescale. The softness ratio also shows a slow decline across the observation, due to a combination of the different time-variability of the power-law continuum and soft hump flux on timescales of ~ 1 week.

Our timing analysis and time-selected spectroscopy indicate that the X-ray emission originates within 12 Schwarzschild radii. The amplitudes and timescales of the rapid variations we observed are consistent with those expected within disk-corona models. Furthermore, the observed fast variability of the soft hump rules out an origin of the soft emission in large scale components, such as circumnuclear starburst. The Γ–soft hump correlation is consistent with the soft hump being produced by up-scattering of the accretion disk radiation within a patchy, flaring disk corona.

Subject headings: galaxies: active – galaxies: individual (Ton S180) – galaxies: nuclei – galaxies: Seyfert – X-rays: galaxies

1. INTRODUCTION

The population of Seyfert 1 galaxies has a widely-used sub-classification into narrow-line Seyfert 1 galaxies (NLS1s) and broad-line Seyfert 1 galaxies (BLS1s). While the scheme appears to make an arbitrary distinction based primarily upon the widths of the optical emission lines (NLS1s having H$\beta \lesssim 2000$ km s^{-1}, Goodrich 1989), this turns out to be an extremely useful terminology as the X-ray properties of the two sub-classes are systematically different. Rapid and large-amplitude variability (Boller, Brandt, & Fink 1996, hereafter BBF96; Turner et al. 1999) is a characteristic of NLS1s, with the excess variance (Nandra et al. 1997a) typically an order of magnitude larger than that observed for samples of BLS1s with the same luminosity distribution (Turner et al. 1999; Leighly 1999a). Spectral properties also vary across the Seyfert population with NLS1s showing systematically steeper photon indices than those of BLS1s across both soft and hard X-ray bands, (Boller, Brandt, & Fink 1996; Brandt, Mathur, & Elvis 1997; Turner, George, & Nandra 1998; Leighly 1999b; Vaughan et al. 1999b). The anti-correlations between Hβ FWHM and both X-ray spectral slope (Boller, Brandt, & Fink 1996; Laor et al. 1997) and excess variance (Turner et al. 1999) reveal a continuous range of parameter values between the NLS1 and BLS1 extremes of the population; the observed differences are now thought to be driven by a range in a fundamental physical parameter, such as the accretion rate.

A popular idea, originally proposed by Pounds, Done, & Osborne (1995), draws an analogy between Seyfert 1 galaxies and Galactic black-hole candidates. The latter show steepening in the high state. In this scenario, NLS1s are sources in the high-state, emitting at higher fractions of their Eddington luminosity, hence having higher fractional accretion rates ($\dot{m} = \dot{M}/\dot{M}_{\rm Edd}$). Given that NLS1s have comparable luminosity to that of the BLS1s, it has often been suggested that they also have relatively small central black holes, i.e., $M_{\rm BH} \approx 10^6 M_\odot$, as opposed to $M_{\rm BH} \approx 10^8 M_\odot$, which is typical for BLS1s (e.g., Peterson et al. 2000; Kaspi et al. 2000). Smaller black-hole masses naturally explain both the narrowness of the optical emission lines, which are generated in clouds that have smaller Keplerian velocities—hence smaller widths—and the extreme X-ray variability, since the primary emission would originate in a smaller region around the central engine (e.g., Laor et al. 1997).

Higher accretion rates lead to some observational predictions, such as a hotter accretion disk leading (via inverse Compton scattering) to enhanced soft X-ray emission and an ionized surface for the accretion disk (Matt, Fabian, & Ross 1993). Support for the ionized disk is found in the form of Kα emission from ionized states of Fe in six NLS1s (Comastri et al. 1998, Turner, George, & Nandra 1998, Vaughan et al. 1999a, Comastri et al. 2001, Turner, George, & Netzer 1999; Ballantyne, Iwasawa, & Fabian 2001). However, the observation of

[1] Department of Astronomy, Ohio State University, 140 West 18th Avenue, Columbus, OH 43210; promano@astronomy.ohio-state.edu, mathur@astronomy.ohio-state.edu.

[2] Joint Center for Astrophysics, University of Maryland, Baltimore County, Department of Physics, 1000 Hilltop Circle, Baltimore, MD 21250; turner@lucretia.gsfc.nasa.gov, ian.george@gsfc.nasa.gov.

[3] Laboratory for High Energy Astrophysics, Code 660, NASA/Goddard Space Flight Center, Greenbelt, MD 20771

similar lines in some BLS1s, may point to the luminosity of the central source playing as important a role as accretion rate (e.g., Guainazzi et al. 1998).

Alternative explanations of the extreme properties in NLS1s are that (1) the broad-line regions (BLR) of NLS1s have larger radii (i.e., the BLR gas is more distant from the nucleus) than in the BLS1s (Guilbert, Fabian, & McCray 1983; Mason, Puchnarewicz, & Jones 1996; Wandel & Boller 1998) then the narrow width of the lines is a reflection of the lower orbital velocity; (2) the NLS1s may be low-inclination (i.e., observed nearly face on) systems (Osterbrock & Pogge 1985). Assuming the motions around the central source to be virialized, the narrowness of the lines is due to the fact that the gas is moving preferentially on a plane that is almost perpendicular to the line of sight, hence the line widths are reduced by a factor of $\sin i$, where $i = 0$ is face-on. One way to distinguish between these models is to measure the the size and virial mass of the BLR via reverberation techniques (Peterson 1993); Kaspi et al. (2000) and Peterson et al. (2000) find that the BLRs of NLS1s and BLS1s have comparable size, while NLS1s have virial masses one order of magnitude smaller than BLS1s, but cannot exclude the second model solely on the basis of reverberation results. However, Boroson & Green (1992) and Kuraszkiewicz et al. (2000) disfavor the low-inclination model, while Nandra et al. (1997b) show that the inner regions of BLS1s also appear to be observed close to face-on.

Tonantzintla (Ton) S180 (PHL 912) is a bright NLS1 with a low Galactic column density along the line-of-sight ($N_H = 1.52 \times 10^{20}$ cm^{-2}; Stark et al. 1992). This source has FWHM Hα and H$\beta \sim 900$ km s^{-1} and a redshift z=0.06198 (Wisotzki et al. 1995). Ton S180 has a relatively high luminosity, with absolute magnitude $M_B = -23.1$ mag.

Ton S180 was observed by *ASCA* on 1999 December 3 to 15, during a multi-wavelength monitoring campaign that included observations from *HST, RXTE, Chandra, EUVE, FUSE*, in addition to optical–IR observations obtained from ground-based observatories. The results of the long-baseline timing project using *RXTE, EUVE* and *ASCA* are reported in Edelson et al. (2001). The *HST* and *FUSE* data were obtained contemporaneously with *Chandra* and *ASCA* and were undertaken to determine the spectral-energy-distribution of the source, as reported in Turner et al. (2001c). The *Chandra* spectral result is reported in Turner et al. (2001a). In this paper we present the results from the ~ 400 ks *ASCA* observation of Ton S180. This long observation has allowed us to study the variability of the spectral components on different timescales, from 12 days to ~ 1 day. This is particularly interesting since the results of a 35-day long observational campaign on the NLS1 Arakelian (Akn) 564 indicate that superimposed on a fast-varying continuum component that dominates the spectrum is a slower-varying soft excess emission (Turner et al. 2001b; Edelson et al. 2001). In §2 we describe our observations and data reduction. In §3 we discuss the time variability of the source. In §4 we analyze the mean spectrum and in §5 we discuss time-resolved spectroscopy. In §6 we present a summary of our observational results, and in §7 a comparison with the properties of Akn 564. Finally, in §8 we discuss the results.

2. OBSERVATIONS AND DATA REDUCTION

The focal-plane instruments on board *ASCA* comprised two CCDs (the Solid-state Imaging Spectrometers SIS0 and SIS1, 0.4–10 keV, Burke et al. 1991) and two gas-scintillation proportional-counters (Gas Imaging Spectrometers GIS2 and GIS3, 0.7–10 keV, Ohashi et al. 1996, and references therein); these were operated simultaneously. *ASCA* observed Ton S180 for a total of ~ 1 Ms, starting on JD 2451516.051 (for the screened data, see below). The data were reduced using standard techniques as used for the *Tartarus*[4] database (Turner et al. 1999). Data screening yielded an effective exposure time of 338 ks for SIS0, 368 ks for the SIS1, and 405 ks for both the GISs. The mean SIS0 count rate was 0.586 ± 0.001 cts s^{-1} (0.5-10 keV band).

Increased dark current levels and decreased charge transfer efficiency (CTE) have become evident in the SIS detectors since ~ 1993, causing a divergence of SIS and GIS spectra. The degradation is not completely understood and at the time of writing not corrected for by any of the software (specifically, CORRECTRDD does not correct for the effect). The instruments can diverge by as much as 40% for energies < 0.6 keV for data taken in 2000 January[5]. The Ton S180 data were calibrated using the latest calibration file released on 2001 March 29 ($sisph2pi\_290301.fits$). The divergence of the SIS detectors at low energies can be compensated for in the spectral analysis. Yaqoob et al. (2000)[6] provide a quantification of the apparent loss in SIS efficiency as a function of mission-elapsed time. The efficiency loss can be parameterized as a time-dependent absorption term ("excess N_H"). The correction for SIS0 follows a linear relationship, $N_H(\mathrm{SIS0}) = (\mathrm{T} - 3.0174828 \times 10^7) \times 3.635857508 \times 10^{12}$ cm^{-2}, where T is the average of start and stop times of the observation, measured in seconds since launch. The SIS1 excess absorption term does not follow the simple linear form found for SIS0 but it is usually found that a slightly larger absorption column can be applied to the SIS1 data to bring it into line with SIS0. For our observations, where $\mathrm{T} = 2.19 \times 10^8$ s, $N_H(\mathrm{SIS0}) = 6.9 \times 10^{20}$ cm^{-2} and we adopted $N_H(\mathrm{SIS1}) = 1.0 \times 10^{21}$ cm^{-2}. Application of the excess N_H correction is important for this analysis, as it allows us to use the valuable data at energies < 1 keV to examine the spectral variability of an interesting spectral component.

3. THE TIME VARIABILITY

Light curves were extracted using bin sizes of 256 s and 5760 s in the full-band (0.7-10 keV) for the SIS, the soft-band (0.7–1.3 keV) for the SIS data, and the hard-band (2–10 keV) for both GIS and SIS data. We adopted 0.7 keV as a lower limit for the SIS data, as appropriate for the setting of the SIS lower level discriminator for these observations. Light curves were constructed combining data from the SIS and GIS detector pairs. The exposure requirements for the combined light curves ensured the bins be fully exposed in each instrument for the 256 s curves and at least 10 % exposed for the 5760 s curves. The observed count rates correspond to a mean 2–10 keV flux of $F_{2-10} = 6.5 \times 10^{-12}$ ergs s^{-1} cm^{-2} and 2–10 keV luminosity $L_{2-10} = 4.9 \times 10^{43}$ ergs s^{-1} ($H_0 = 75$ km s^{-1} Mpc^{-1}, $q_0 = 0.5$).

---

[4] http://tartarus.gsfc.nasa.gov

[5] see http://heasarc.gsfc.nasa.gov/docs/asca/watchout.html

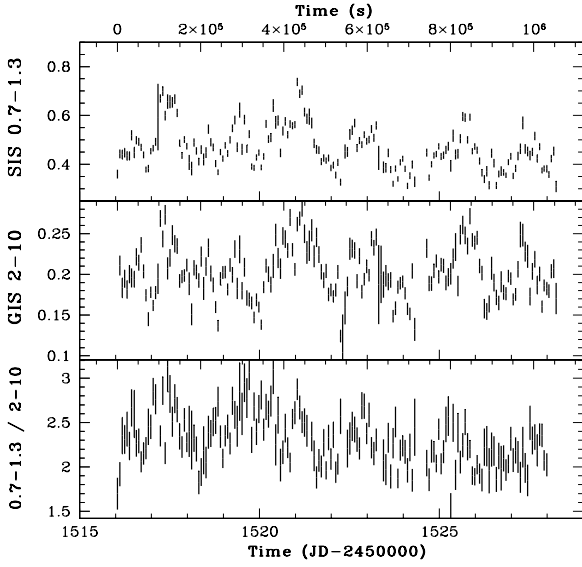[6] see http://lheawww.gsfc.nasa.gov/~yaqoob/ccd/nhparam.html

Fig. 1.— Light curves for the *ASCA* data in cts s^{-1} and in 5760 s bins. The top panel is the SIS soft band (0.7–1.3 keV) light curve; the middle panel the GIS hard band (2–10 keV) and the bottom panel is the ratio of 0.7–1.3/2–10 keV. The background level in the source cell is about 4 % and 10 % of the SIS and GIS source count rates, respectively, and not plotted. The times are reported both in seconds from the start of exposure (top axis) and in JD−2450000 (bottom axis).

This mean flux level is ∼ 20 % brighter than that observed during a previous *ASCA* observation on 1996 July 10 (Turner, George, & Nandra 1998). Figure 1 shows the combined 0.7–1.3 keV SIS soft-band and GIS hard-band light curves in 5760 s bins. The background levels in the source cells are about 4% and 10% of the SIS and GIS source count rates, respectively, and not plotted, or subtracted. Figure 1 also shows the softness ratio, defined as the ratio between the count rates in the 0.7–1.3 and 2–10 keV bands. There is significant hardening of the spectrum during the observation, and the softness ratio changes by ∼ 20 %.

The light curves integrated to 5760 s show trough-to-peak flux variations by a factor of ∼ 2.7 in the 0.7–1.3 keV band (SIS), ∼ 2.4 in the 2–10 keV band (GIS). The light curves sampled on 256 s reveal even larger amplitudes due to fast flickering, with a maximum amplitude of variability of a factor ∼ 3.5 for the SIS data in the 0.7–1.3 keV band and ∼ 3.9 for the GIS data in the 2–10 keV band. Figure 2 shows the 0.7–1.3 and 2–10 keV light curves in 256 s bins for three rapid "events" centered around 603, 608, and 614 ks from the start of the observation (JD 2451523.03, 2451523.08, and 2451523.16). In the first event the soft and hard-band data show a variations (trough-to-peak) of factors of R_{max}(SIS) = 1.32 ± 0.13 and R_{max}(GIS) = 1.80 ± 0.38, respectively, in Δt = 1972 s (the errors on R_{max} are obtained propagating the errors in the light-curve points). In the second event R_{max}(SIS) = 1.34 ± 0.13 and R_{max}(GIS) = 1.75 ± 0.37, respectively, in Δt = 1972 s. In the third event, the variation is a factor of R_{max}(SIS) = 1.33 ± 0.13 for the soft while the hard is consistent with a constant. These events correspond to a variation in luminosity of ΔL = 2.4 ± 0.9 × 10^{43} ergs s^{-1} (as calculated from SIS data, from the first event; GIS data yield ΔL = 2.6 ± 0.9 × 10^{43} ergs s^{-1}). In the first and sec-

ond events the hard X-ray flux variation is sharper than that in the soft band, and there is a change in the softness ratio, in the sense that when the flux increases the spectrum hardens, with a timescale of ∼ 1000 s (Figure 2, bottom panel). However, in the third event a flux change is not accompanied by a strong spectral change. Further examination of the light curves reveals other examples of diverse variability behavior with no obvious general trend. This is a behavior previously reported in *ROSAT* observations (Fink et al. 1997).

The soft and hard X-ray light curves in Figure 1 exhibit similar characteristics, suggesting a short time delay between the variations in each curve. To quantify any correlations we undertook a cross-correlation analysis using the interpolation cross-correlation function (ICCF) method of Gaskell & Sparke (1986) and Gaskell & Peterson (1987) as implemented by White & Peterson (1994). We calculated the CCFs of the total hard-flux in the 2–10 keV band with respect to the total soft-flux in the 0.7–1.3 keV band, which has the highest signal-to-noise. The CCFs are sampled at a resolution of 0.05 day, and the centroids are computed using all points near the peak of the CCFs with values greater than 80% of the maximum value of the correlation coefficient, r_{max}. The 1-σ uncertainties quoted for the ICCF centroid, τ_{cent}, are based on the model-independent Monte Carlo method described by Peterson et al. (1998). We obtain r_{max} = 0.748 and τ_{cent} = 0.025$^{+0.024}_{-0.002}$ days. Given the 180 points in our light curves, the probability of exceeding r_{max} ≈ 0.3 from uncorrelated samples is ≪ 0.1 %, and the lag is less than 0.07 d at 95 % confidence. Since the power-law component provides ∼ 72 % of the flux in the mean spectrum 0.7–1.3 keV band, as we will show in §4.1, and the power-law component dominates the 2–10 keV band, this correlation is probably dominated by the rapid variability in the power-law flux.
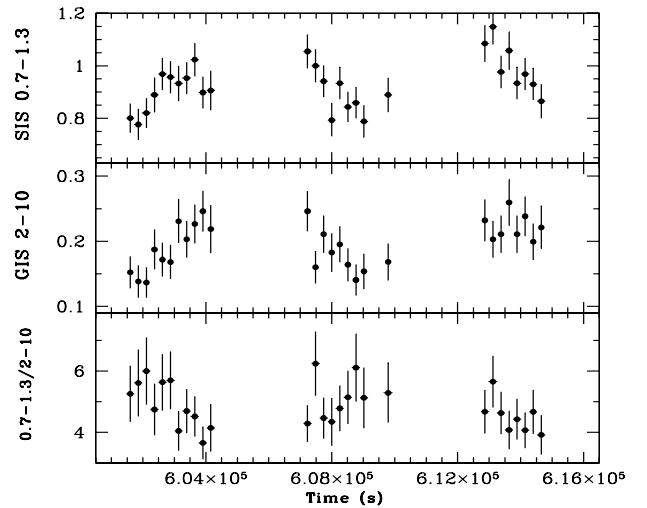

Fig. 2.— Same as Figure 1, for two "events" at JD ≈ 2451523. The time is seconds from the start of observation, the bin size is 256 s. In the first and second event, the SIS and GIS data show a variations up to a factor of 2 in Δt = 1790 s; in the third event, the variation is of a factor of ∼ 1.3 in Δt = 1536 s (§3).
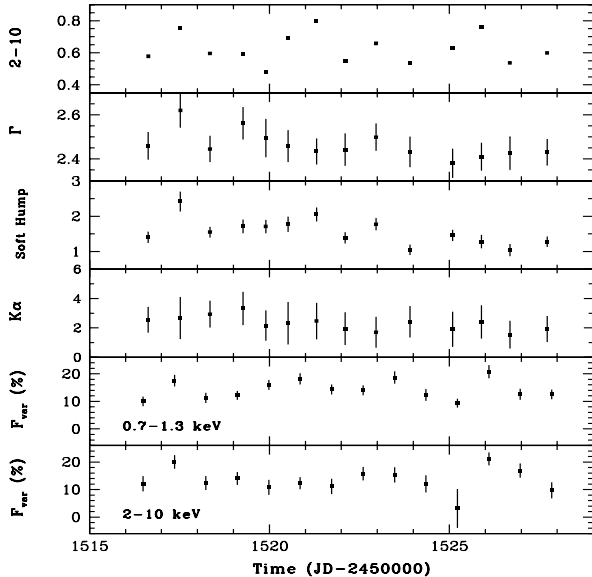
FIG. 3.— Spectral and timing parameters obtained from fits to the individual time-resolved spectra. From the top, the light curves are the (model) continuum flux in the hard band, the photon index Γ, the soft hump flux, the Kα flux (laor), the fractional variability F_{var}. The continuum fluxes are in units of 10^{-11} ergs s^{-1} cm^{-2}, the soft hump flux in units of 10^{-2} photons s^{-1} cm^{-2} and the Kα flux in units of 10^{-5} photons s^{-1} cm^{-2}.

3.1. Fractional Variability Amplitude

The fractional variability amplitude F_{var} and its error $\sigma_{F_{var}}$ are defined in Edelson et al. (2001), as

$$F_{var} = \sqrt{\frac{S^2 - \langle \sigma_{err}^2 \rangle}{\langle X \rangle^2}}, \qquad \sigma_{F_{var}} = \frac{1}{F_{var}} \sqrt{\frac{1}{2N} \frac{S^2}{\langle X \rangle^2}}. \qquad (1)$$

where S^2 is the total variance of the light curve, $\langle \sigma_{err}^2 \rangle$ is the mean squared error, and $\langle X \rangle$ is the mean count rate.

First we calculated F_{var} across the baseline of the entire observation. This quantity measures deviations compared to the mean, integrated over the entire 12 days. We measured this quantity in the soft (0.7–1.3 keV) and hard (2–10 keV) bands, using our light curves with 256 s bins. These bands were chosen to sample energy ranges containing different spectral components (see §4) while still maintaining good signal-to-noise. F_{var} thus calculated is $19.12 \pm 0.58\%$ in the 0.7–1.3 keV band, and $17.26 \pm 0.65\%$ in the hard-band, using SIS data for both tests.

To examine the evolution of timing properties of Ton S180 further, we split the data into 14 evenly-sampled sections across the 12 day *ASCA* observation. Even sampling is important because F_{var} depends strongly on the duration of the data-train. The baseline for each time-selected section of data was 75 ks with average on-source exposure time 25 ks. We then calculated F_{var} over each of these one-day intervals (again with 256 s bins in each "daily" light curve"). This test showed that F_{var} is significantly variable showing correlated changes in the soft and hard bands, on a day-to-day basis (figure 3).

As we will demonstrate in §4.1, in the mean spectrum the power-law continuum provides about 72 % of the flux in the 0.7–1.3 keV band, and the power-law variations contribute significantly to F_{var} in both the soft and hard bands, explaining the gross similarity between the quantity in those two bands. The
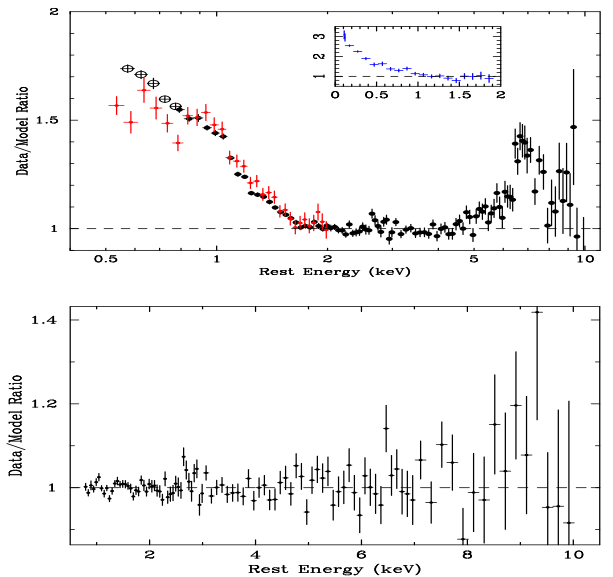

FIG. 4.— Top: Data/Model ratio where the model is a simple power law fit to the 1.8–4.71 keV data (observer's frame). The rest of the combined SIS and GIS data are then overlaid, revealing a strong soft hump and Fe emission line, as filled circles. The 0.5–0.7 keV SIS data, though not used, are also plotted as empty circles. The crosses are the *ASCA* data from 1996 below 2 keV. The inset panel shows the *ROSAT* PSPC data compared to the continuum power law, illustrating the shape of the soft hump at lower energies (§4). All datasets confirm the presence of the soft hump, and detail its shape. Bottom: Data/Model ratio where the model is a power law plus soft hump (Gaussian; §4.1) plus 2-Gaussian model for the Fe Kα line (§4.2).

slightly greater F_{var} for the soft band is probably due to a combination of changes in the relative flux levels of two spectral components (power law and hump), and slope changes in the power-law, as we will show in §5.3.

4. THE MEAN SPECTRUM

Source counts were binned with a minimum of 20 counts per energy bin for the spectral analysis. The data from the four instruments were fit simultaneously, with the relative normalizations free to allow for small differences in calibration of the absolute flux and in the fraction of encircled counts encompassed by the SIS versus GIS extraction cells. Spectral fits were performed using XSPEC V11.0.1 and response files generated with HEASoft v5.0.4. Ton S180 is detected at better than 3-σ level in the SIS data for energies $\lesssim 7.5$ keV and in the GIS data for energies $\lesssim 9.5$ keV (observed frame, in the unbinned spectrum).

The photon index Γ (defined by photon flux $P_E \propto E^{-\Gamma}$) was determined by fitting a power-law model attenuated by Galactic absorption with an additional correction applied to SIS0 and SIS1 to compensate for the low-energy degradation as described in §2. For this fit we used data in the bandpass 1.8–4.71 keV (observer's frame). The power-law fit yielded $\Gamma = 2.44 \pm 0.02$ and $\chi^2 = 720$ for 683 degrees of freedom (*dof*). Inclusion of the data in the 7.06–9.42 keV bandpass produces consistent results. This and subsequent errors represent, unless otherwise specified, the 90 % confidence level.

The data/model ratio is shown in Figure 4, top panel. A strong soft excess is evident, appearing as a hump of emission rising above the power-law continuum at energies < 2 keV. This

feature was also observed in the *ROSAT* PSPC observations (Fink et al. 1997, inset in top panel of Figure 4), *BeppoSAX* observations (Comastri et al. 1998), and the earlier *ASCA* observation (sequence number 74081000; Turner, George, & Nandra 1998). Hereafter we refer to this component as the "soft hump". Also evident in the main panel is an excess of emission close to 7 keV, which is due to an unmodeled Fe Kα emission line.

Minor calibration problems are visible in such high signal-to-noise data at ≈ 1.7–3.0 keV. They are not so serious as to warrant exclusion from the fit. We note, however, that they contribute significantly to the χ^2 in the soft component fits (§4.1) and to a lesser extent to the Kα fits (§4.2).

4.1. *The Soft Component*

We confirm the presence of the soft X-ray emission component previously observed by Fink et al. (1997), Comastri et al. (1998), and Turner, George, & Nandra (1998). At the time of writing, the status of the SIS calibration limits the accuracy to which the absolute form of the soft spectral hump can be determined. Thus we adopted a simple parameterization of the soft hump which allowed us to perform a sensitive examination of the flux variability of the component. The simultaneous *Chandra* LETG data for Ton S180 (Turner et al. 2001a) and the results for NGC 4051 (Collinge et al. 2001) show that the soft hump is a smooth continuum component, as opposed to a blend of unresolved spectral features. The variability study afforded by the *ASCA* data is therefore the optimum available tool for exploring the nature of the soft hump. This was also shown to be the case for Akn 564 (Turner et al. 2001b).

We used SIS data in the range 0.7–4.71 keV simultaneously with GIS data in the range 1.0–4.71 keV (observer's frame). The lower energy limit of the SIS data was based on the level of agreement achieved between the two CCDs using our methods of correction (§2). The upper energy limit of both SIS and GIS effectively excluded the Fe Kα regime for these fits, in order to avoid an overly complex model (which can result in false or local minima being found). A steep power-law component is an inadequate representation of this excess, as its form shows some curvature. The Gaussian model which best fits the soft hump has an energy of the peak $E = 0.17^{+0.17}_{-0.17p}$ keV (the energy pegged at the lower limit), full width at half maximum FWHM $= 1.01^{+0.05}_{-0.12}$ keV and flux $1.50^{+0.37}_{-0.61} \times 10^{-2}$ photons s^{-1} cm^{-2} corresponding to a mean equivalent width EW $= 94^{+23}_{-38}$ eV. For this fit $\chi^2 = 1069$ for 896 dof, but there is a contribution to the χ^2 from the ≈ 2.5–3.0 keV region due to calibration problems (see §4). Significantly inferior (to better than 99.9 % confidence; $\chi^2 = 1096$ for 897 dof) is a parameterization of the soft hump as a blackbody model; the best fit that yielded a rest-frame temperature $kT = 153^{+2}_{-3}$ eV, flux $1.07^{+0.03}_{-0.04} \times 10^{-4}$ photons s^{-1} cm^{-2}, and absorption corrected luminosity in the 0.7–1.3 keV band $L_{0.7-1.3} = 1.6 \times 10^{43}$ ergs s^{-1}.

Using a Gaussian parameterization of the soft hump, we determined that the power-law continuum contributes to $\sim 72\%$ of the flux in the soft (0.7–1.3 keV) band of the mean spectrum. We also retrieved the 1996 ASCA spectrum (Turner, George, & Nandra 1998) from the *Tartarus* database (Turner et al. 1999), and found consistent contributions of the different spectral components to the soft band over the same energy ranges as we used for our 12-day observation.

TABLE 2
SPECTRAL FITS IN THE 2–10 KEV BAND.

Model	Γ^a_{2-10}	$E^{a,b}_{\rm Fe}$ (keV)	EW^a (eV)	χ^2/dof
(1)	(2)	(3)	(4)	(5)
PL^c	2.37 ± 0.01	...	...	1518/1372
PL + DISKLINE	$2.43^{+0.01}_{-0.02}$	$6.40^{+0.27}_{-0.00p}$	461^{+120}_{-84}	1353/1368
PL + LAOR	2.43 ± 0.02	$6.55^{+0.16}_{-0.15p}$	517^{+123}_{-111}	1352/1368
PL + NG	2.39 ± 0.01	$6.75^{+0.08}_{-0.04}$	182^{+30}_{-26}	1404/1370
PL + BG	2.44 ± 0.02	$6.71^{+0.12}_{-0.14}$	550^{+184}_{-128}	1352/1369
PL + BG + NG	$2.46^{+0.03}_{-0.02}$	$6.58^{+0.25}_{-0.28}$	512^{+225}_{-136}	1328/1359
		$6.81^{+0.08}_{-0.12}$	90^{+33}_{-31}	

^{a} 90 % confidence level uncertainties.

^{b} Rest frame of Ton S180.

^{c} Over the whole hard energy range. The value of the photon index from the continuum fit is 2.44 ± 0.02 (§4).

4.2. *The Fe Kα Regime*

Comastri et al. (1998) and Turner, George, & Nandra (1998) found evidence for line emission at ~ 7 keV, indicative of an origin from material containing ionized iron, consistent with the iron line from H-like iron at 6.94 keV. Hence, having found an adequate parameterization of the continuum shape (in the 1.8–4.71 keV band), we included the 4.71–7.45 keV SIS data and the 4.71–9.42 keV GIS data in the analysis and examined the data/model ratio (versus the best-fit continuum model, top panel of Figure 4). The mean line profile is broad and asymmetric, similar to that observed in the previous *ASCA* observation (Turner, George, & Nandra 1998).

We utilized the SIS data in the 1.8–7.45 keV range simultaneously with the GIS data in the 1.8–9.42 keV range. Table 4.1 summarizes our results: Column (1) lists the models, Column (2) the photon index, Column (3) the rest-frame energy of the fitted Fe line, Column (4) its equivalent width, and Column (5) χ^2 and degrees of freedom relative to the fit. PL indicates the power-law continuum, BG the broad Gaussian, and NG the narrow Gaussian (see details below).

The asymmetry of the profile prompted us to fit the iron Kα line using the `diskline` model profile of Fabian et al. (1989). This model assumes a Schwarzschild metric, with an emissivity law r^{-q} for the illumination pattern of the accretion disk, where r is the radial distance from the black hole. We adopted $q = 2.5$ based upon the results of Nandra et al. (1997b). We also assume that the line emission originates within 1000 gravitational radii ($R_{\rm g} = GM/c^2$). The inclination of the system is defined such that $i = 0$ is a disk oriented face-on to the observer. Fits using this model yielded $\chi^2 = 1353$ for 1368 dof. The rest-energy of the line was $E = 6.40^{+0.27}_{-0.00p}$ keV, the inner radius was $r = 6^{+10}_{-6p}$ $R_{\rm g}$, the inclination was $i = 35^{+22}_{-35p}$ degrees, and flux $2.06^{+0.54}_{-0.37} \times 10^{-5}$ photons s^{-1} cm^{-2}. The equivalent width was EW $= 461^{+120}_{-84}$ eV.

We also tested a model for the line profile assuming a Kerr metric for a maximally rotating black hole as implemented by Laor (1991). This will have the most intense gravitational effects. We fixed the emissivity index as for the Schwarzschild case and the outer radius at the maximum value allowed by the model, 400 $R_{\rm g}$. Using the same energy restriction as for the Schwarzschild model, the Kerr model provides a fit-statistic $\chi^2 = 1352$ for 1368 dof. The rest-energy of the line was $E = 6.55^{+0.16}_{-0.15p}$ keV, inclination was $i = 23^{+14}_{-23p}$ degrees, and flux $2.22^{+0.53}_{-0.47} \times 10^{-5}$ photons s^{-1} cm^{-2}. The equivalent width was EW $= 517^{+123}_{-111}$ eV.
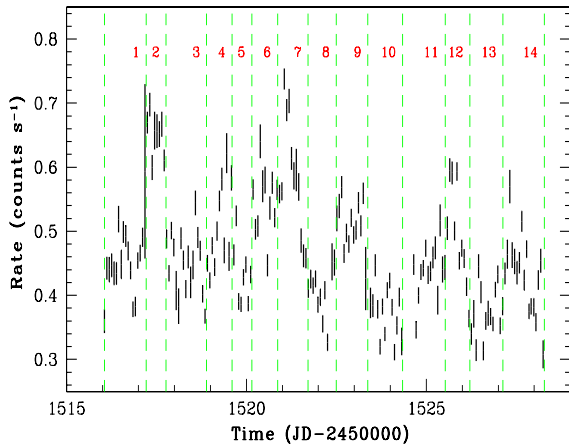
FIG. 5.— Combined SIS 0.7–1.3 keV light curve in cts s^{-1} and in 5760 s bins. The background level in the source cell is about 4 % of the source count rate, and not plotted or subtracted. The vertical dashed lines show our 14 time intervals within which spectra were extracted (§5). The "flares" shown in Figure 2 (§3) are within bin 9.

The line was better fit as the sum of a broad and a narrow redshifted Gaussian profile, with $\chi^2 = 1328$ for 1359 dof (a broad or narrow Gaussian alone are a significantly worse fit at > 99 % confidence; see Table 4.1). The rest energy of the narrow line (fixed at 10 eV width) was $E_N = 6.81^{+0.08}_{-0.12}$ keV, with EW = 90^{+33}_{-31} eV. The broad component gave $E_B = 6.58^{+0.25}_{-0.28}$ keV and EW = 512^{+225}_{-136} eV. The residuals of the 2-Gaussian fit are shown in the bottom panel of Figure 4. Some excess emission is evident in the 8–9 keV region. However, the signal-to-noise in this energy range is so low (the detection level is $\sim 3\,\sigma$) that no meaningful spectral fit can be performed.

We do not detect any narrow (fixed at 10 eV width) Kα emission at rest energy 6.4 keV, in addition to the Schwarzschild, Kerr, single broad Gaussian, or 2-Gaussian models.

5. SPECTRAL VARIABILITY

5.1. *Method and Selection Details*

To examine the spectral evolution of Ton S180, we created 14 time-selected spectra across the 12 day *ASCA* observation by sampling throughout the light curve following flares and dips with Xselect V2.0. The resulting average baseline for each time-selected spectrum was 75 ks, for an average on-source exposure time 25 ks. Our choice of intervals is shown in Figure 5. The "events" described in §3 (Figure 2) occur during time bin 9. Background, ancillary response, and response matrix files were set to be those of the mean spectrum. The background spectrum and flux did not vary significantly during the observation and use of the mean spectra yielded the best possible signal-to-noise for the time-resolved spectroscopy. Again, spectra were binned to achieve a minimum of 20 counts per energy bin. We performed all fits by fixing the scaling factors for instrument normalization based upon the fits to the mean spectrum. Corrections for the SIS low-energy problem were fixed at the same values used for the mean spectrum. All models were modified with a Galactic absorption. Time assignments for the spectra refer to the mid-point of the observation, in JD − 2450000. The results of our analysis are shown in Figure 3 in the form of time series curves for the various parameters. These are described in detail in the following sections.
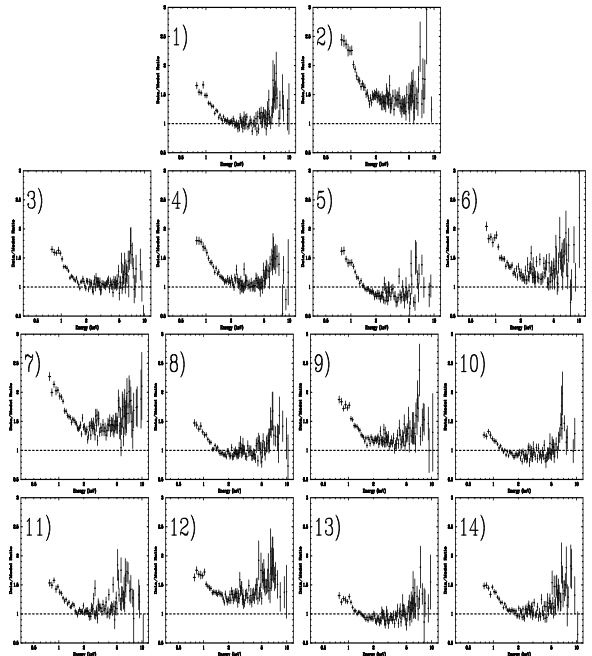

FIG. 6.— Ratio plots obtained by fitting the best-fit model for the first spectrum to the following 13 spectra. Energy ranges and instrument utilized are described in §5.2. Energies are in the rest frame of Ton S180.

5.2. *Variability of the Continuum*

We fit each of the 14 time-selected spectra in the 1.8–4.71 keV range (both SIS and GIS; observer's frame) with a simple power-law model. The light curves for the (model) continuum flux and the best-fit photon index Γ are shown in Figure 3. The photon index Γ, thus sampled on a ~ 1 day timescale, ranges in 2.38–2.62 (i.e., $\Delta\Gamma = 0.24$) across the 12 days, but these variations are not significant (fitting the photon indices to a constant model yields $\chi^2 = 10$ for 13 dof). Therefore, the rapid flux variability evident on timescales as short as ~ 1000 s in the hard band (Figure 2, §3) is not due to changes in Γ, but is truely flux changes in that band. However, on longer timescales of about a week significant changes in Γ occur, as we will show in §5.3.

Figure 6 shows ratio plots obtained by comparing the best-fit model for the first spectrum to the following 13 spectra, without performing any fit. The plot illustrates the variations of the spectral shape and flux compared to the first day of data. Strong variations in the flux and, to a lesser degree, in the continuum slope are evident. The soft hump is always present superimposed on the power-law continuum, although it appears to change in absolute strength, relative to the power-law continuum and possibly in shape (see, for example time-cuts 2 and 13) on a timescale of approximately a day. Variations in the shape of the soft hump, however, are a minor effect compared to the flux variations of the soft hump.
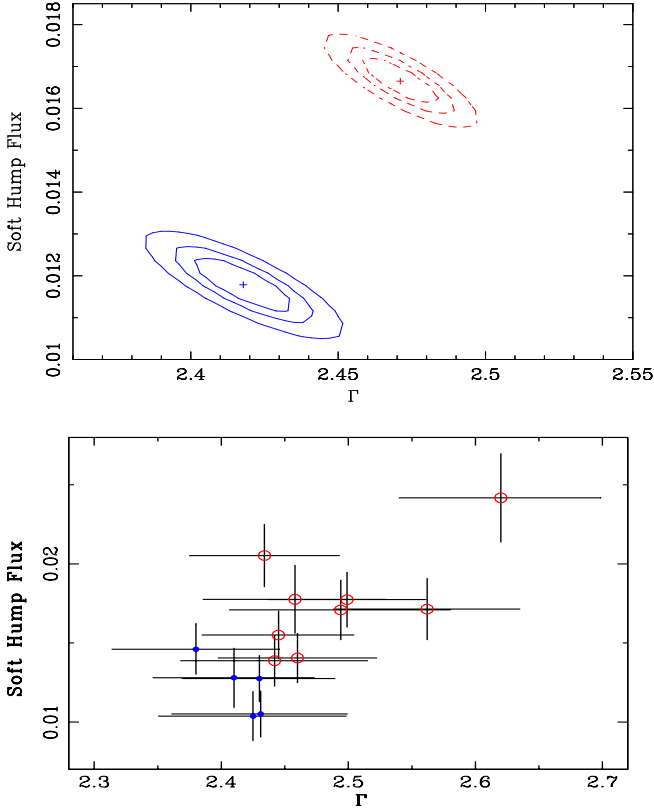
of the observation (see Figure 1). Fits were performed on each state, as we did for the mean spectrum (§4.1), and confidence contour plots were generated for the flux of the soft hump versus the photon index, assuming the soft hump shape to be approximately constant during the observation. The resulting Γ–soft hump flux contours are well separated (Figure 7, top) in both directions. Hence, the confidence contour plot indicates that the source varies significantly in photon index *and* strength of the soft hump on a timescale of about one week. Therefore both effects are contributing to the change in softness ratio observed across the baseline of the observation. The spectral changes observed between the soft and hard states result in a change of the EW of the soft hump from $EW_{\mathrm{soft}} = 100 \pm 5\,\mathrm{eV}$ to $EW_{\mathrm{hard}} = 84^{+6}_{-7}\,\mathrm{eV}$.

Since we adopt a fixed soft hump shape in our fits of the 14 time-selected spectra, we are confident our fitting method can separate the fluxes of soft hump and power-law continuum. Furthermore, the bottom panel in Figure 7 shows Γ plotted against the strength of the soft hump component and demonstrates a strong correlation (Spearman rank coefficient $r_s = 0.68$, probability of chance occurrence is 8×10^{-3}), as is expected from disk-corona models, as we will see in §8. If the strength of the soft hump component and the photon index were difficult to separate in the spectral fit, we would expect an anticorrelation instead. Figure 7 also shows that a steeper photon index appears to be associated with a relatively strong soft hump. Finally, as noted in §5.2, the variations in the shape of the Gaussian soft hump are small so that our model for the soft hump parameterizes most of the flux in each time-selected spectrum, and does not weaken our approach in fixing the shape when testing for flux variability.

FIG. 7.— Top panel: the $\Delta\chi^2 = 2.3, 4.61, 9.21$ contour levels for the soft hump flux (in units of photons s^{-1} cm^{-2}) vs. photon index Γ. The full contours correspond to the hard state (§5.4), the dashed contours to the soft state, and crosses indicate the best-fit values. Bottom panel: the strength of the soft hump plotted against photon index Γ in our 14 time-selected spectra with high-state (open circles) and low-state (filled circles) points overlaid.

5.3. *Variability of the Soft X-ray Hump*

We examined the variability of the soft hump using SIS data in the range 0.7–4.71 keV simultaneously with GIS data in the 1.0–4.71 keV range (observer's frame), as we did for the mean spectrum in §4.1. The model was a simple power-law plus a broad Gaussian for the soft hump, with the Gaussian peak and width fixed at the values noted in §4.1. The flux of the soft hump, the flux of the continuum power law, and the power-law slope were free parameters. The time series for the flux of the soft hump is shown in Figure 3. Fitting a constant model to this flux yields $\chi^2 = 47$ for 13 dof. The soft hump flux varies by a factor of $R_{\mathrm{max}} = 2.33 \pm 0.45$ while the 2–10 keV flux (when binned the same way) varies by a factor of $R_{\mathrm{max}} = 1.65 \pm 0.02$.

In Akn 564, Turner et al. (2001b) showed that the different amplitudes of variability of the soft hump and power-law (6.44 ± 3.30, compared to 3.97 ± 0.06) explain the gross change in softness ratio across the observation. In Ton S180, the amplitude of variation of the soft hump is not so pronounced, although it is clear from the light curves (Figure 3) that most of the flares in the hard X-ray flux are also present in the soft hump. To clarify the situation in Ton S180, we split the data into "hard" and "soft" states based upon the softness ratio. We chose $\mathtt{T} < 6.3 \times 10^5$ s for our soft-state spectrum, and $\mathtt{T} > 6.3 \times 10^5$ s for our hard-state spectrum where $\mathtt{T}$ is the time from the start

5.4. *Variability of the Fe Emission Line*

As we have seen in §5.2, Figure 6 suggests that there are small variations in the strength of the Fe emission line. To investigate this possibility, we utilized SIS data in the 1.8–7.45 keV range simultaneously with the GIS data in the 1.8–9.42 keV range, as we did for the mean spectrum in §4.2. The model was a simple power-law continuum plus different models for the $K\alpha$ line, with fixed shape parameters. We initially tested the assumption of a fixed shape by splitting the data with an intensity division equivalent to an SIS0 count rate of 0.6 cts s^{-1}. This yielded high- and low-state spectra with similar signal-to-noise. We also calculated confidence contours of line flux versus Γ. Figure 8a shows overlapping contours, thus this division of the data, corresponding to a timescale of about 1 week, reveals no evidence for significant flux variability. Using the high and low-state data we then fit for the mean continuum slope as described in §4 and overlaid the data in the $K\alpha$ band relative to the local power-law slope in each case. The two line profiles are shown as data/model ratios in figure 8b and they appear indistinguishable. The same test, performed with the soft- and hard-state division discussed in §5.3, leads us to conclude that no changes were observed either in flux or in shape of the line. Figure 8c,d show the confidence contour and the line profile, respectively, for the soft- and hard-state spectra. We further tested the possibility that the shape of the line might be variable, on a ~ 1 day timescale by overplotting the line profiles for spectra that looked qualitatively different. No significant changes in the line profile are observed.
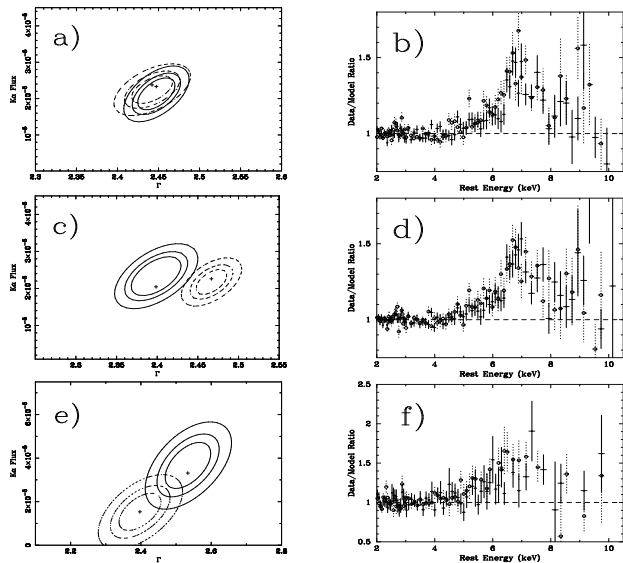
FIG. 8.— Panel a: the $\Delta\chi^2 = 2.3, 4.61, 9.21$ contour levels for Fe K-shell line intensity (in units of photons s^{-1} cm^{-2}) vs. photon index Γ; the full contours correspond to the high state (§5.4), the dashed contours to the low state, and crosses indicate the best-fit values. Panel b: the Fe Kα regime compared to the continuum model; with overlay of high-state (open circles) and low states (filled circles). Panel c: same as a, with full contours corresponding to the hard state (§5.3), dashed contours to the soft state. Panel d: same as b, with hard-state (open circles) and soft-state (filled circles) overlaid. Panel e: same as a, with full contours corresponding to the high Kα flux bin 4 (§5.4), the dashed contours to the low Kα flux bin 13. Panel f: same as b, with bin 4 (open circles) and bin 13 (filled circles) overlaid.

Once assured that variations of the line shape, if present, are minor, we returned to our 14 time-selected spectra, where we considered the following models for Kα line: (1) a `laor` (Kerr) model; (2) a 2-Gaussian model (§4.2) with the two fluxes allowed to vary independently; (3) a 2-Gaussian model in which either the broad Gaussian flux or (4) the narrow Gaussian is flux fixed to the best-fit value from the mean spectrum; and (5) a 2-Gaussian model in which fluxes have fixed ratio derived from fits to the mean spectrum. All fits were performed with photon index and the flux of the power law continuum left as free parameters. The shape of the Kα line was kept fixed to the best fit values obtained for the mean spectrum. No model component was included for the soft hump, as we excluded the soft-band data for these fits. Figure 3 shows the time series for the Kα line for the Kerr model, yielding results similar to those obtained from models (2) through (5). Fits to a constant model yield $\chi^2 = 3$ for 13 dof, thus the line does not show significant changes in flux when sampled on ~ 1 day timescale. Analogous conclusions can be drawn for all other models considered.

Finally, we considered the spectra extracted in bins 4 and 13, which have the highest and the lowest measured Kα flux, respectively (Figure 3). We calculated confidence contours of line flux versus Γ and overplotted the line profiles as we did above. Figure 8e shows the contour plots which demonstrate that the flux variation is insignificant and there is a large overlap of the contours. Figure 8f shows the line profiles, whose large equivalent widths are consistent at 90 % confidence

(EW$_4$ = 889^{+219}_{-368} eV, EW$_{13}$ = 411^{+252}_{-249} eV). Therefore, we do not detect significant variations in EW or flux of the Kα line. With the signal-to-noise available using these data the line flux would have had to vary by at least a factor of 2 for us to detect it at the 99 % confidence level (cf. Figure 8e).

We also applied a `laor` model to the 1996 *ASCA* observation (Turner, George, & Nandra 1998), within the same energy ranges as we used here and with the corrections for the SIS low-energy degradation appropriate to 1996 (see §2), and obtained peak energy, EW, and inclination for the Kα line consistent with what we found in §4.2.

5.5. *RMS Spectra*

In optical/UV spectroscopy of active galactic nuclei, it is easy to obtain a series of spectra of sufficiently high S/N to perform time-resolved spectroscopic analysis. In this case, a useful way to isolate variable features is to construct a root-mean-square (rms) spectrum. This ASCA long look has allowed us to use our 14 individual time-selected spectra described in §5 in analogous way. For each detector the 14 spectra have been rebinned so that each bin has at least a 5-sigma detection (but up to a maximum of 10 adjacent bins were combined to achieve a signal-to-noise ratio of 5 within a bin) then they were degraded to the resolution of the worst spectrum. We created rms and mean spectra by calculating the rms and mean flux in each bin. The choice of a simple mean as opposed to a weighted mean was dictated by the fact that we did not want to favor the high state spectra. Figure 9 shows the ratio rms/mean spectrum for SIS1 and SIS0, using data with energy > 0.7 keV. The mean value is $\sim 20\%$ and there is no systematic trend for different energies. This is consistent with the results from §4.1 showing that the power-law continuum component contributes most of the flux in the hard band and $\sim 72\%$ of the flux in the soft band. The possible weak trend for energies < 2 keV of increased variability for decreasing energy, may suggest that the soft hump is partially driving the variability in the soft band. The "spike-like" features at ~ 1.7–2.5 keV are probably due to calibration uncertainties.
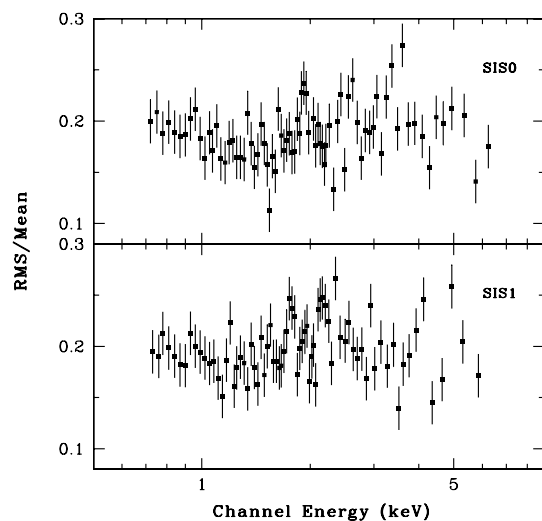

FIG. 9.— The ratio of RMS/Mean spectrum for SIS1 and SIS0, using data of energy > 0.7 keV. The "spike-like" features at ~ 1.7–2.5 keV are probably due to calibration uncertainties.

6. SUMMARY OF OBSERVATIONAL RESULTS

1. On a 12-day baseline, the X-ray flux of Ton S180 presents trough-to-peak variations by a factor 3.5 in the 0.7–1.3 keV band, and 3.9 in the 2–10 keV band when sampled using 256 s bins.

2. The mean photon index, calculated from the continuum fit of the mean spectrum, is $\Gamma = 2.44 \pm 0.02$. Time-resolved spectroscopy reveals significant changes on timescales of ~ 1 week.

3. We confirm the presence of a separate "soft hump" component at energies < 2 keV. This component shows flux variations down to timescales of ~ 1 day, ranging by a factor of 2.3 in normalization over the 12 days of our observations. Some flux changes appear to match changes in the 2–10 keV flux on this timescale although the soft hump shows a drop in EW from 100 to 84 eV across the observation. Minor changes in the shape of the soft hump are apparent on timescales of a few days.

4. In our approximately daily sampling the photon index is correlated with the flux of the soft X-ray hump.

5. Variations in both the photon index and soft hump strength contribute to the change in softness ratio observed across the *ASCA* observation.

6. The softness ratio reveals spectral variability down to timescales of ~ 1000 s in addition to the slow decline across the observation. The power-law and soft hump show divergent behavior on very short (1000 s) or long (2 weeks) timescales.

7. The Fe Kα line emission is detected with a narrow component peaking at ~ 6.8 keV, indicating an origin in ionized material. A broad line component (EW ~ 500 eV) is also evident. We do not detect significant variations of the Fe Kα line strength or equivalent width, on timescales of ~ 1 day–12 days.

7. COMPARISON WITH AKN 564

Comparison of our results for Ton S180 with those obtained for Akn 564 (Turner et al. 2001b) reveals broad similarity in the overall shape of the X-ray spectra (steep power-law continuum, strong soft excess, and ionized, large EW Fe Kα), and variability characteristics. Given these similarities, that may be indicative of the characteristics of the NLS1 as a class, we summarize the properties of these two NLS1s in Table 2. Column (1) lists the properties; Column (2) and (3) the values for Ton S180 and Akn 564, respectively; Column (4) and (5) the references for Ton S180 and Akn 564, respectively.

8. DISCUSSION AND CONCLUSIONS

Ton S180 reaffirms the rapid and large-amplitude X-ray variations which are a characteristic of the NLS1 class. During our 12-day observation, the light curves sampled on 256 s timescales show trough-to-peak flux variations by a factor of ~ 3.5 in the soft band (0.7-1.3 keV), and up to a factor of ~ 4 in the hard band (2–10 keV). Further examination of these light curves shows variations up to a factor of ~ 2 occurring on timescales of ~ 1000 s which are sometimes accompanied by spectral changes. There is a strong correlation ($r_{max} = 0.748$)

between the soft- and hard-band light curves, with a 95 % confidence upper limit on the lag of hard with respect to soft of $\tau_{cent} < 0.07$ d. The strength of this correlation, the short lag, and the fact that ~ 72 % of the flux in the soft band is contributed by the power-law continuum while the hard flux is driven by the power-law, indicate that this correlation is dominated by the variations of the power-law continuum itself.

We used these timing data to obtain an estimate of some fundamental parameters for Ton S180. Our estimate of the accretion efficiency is $\eta \gtrsim 7$ %, marginally above the limit for the efficiency in the Schwarzschild geometry, perhaps favoring a Kerr geometry. However, large uncertainties are associated with this estimate (see Brandt et al. 1999). Light-crossing time arguments yield a radius R for the emitting region, $R \lesssim 12\,R_S$ for $M_{BH} \gtrsim 8 \times 10^6 M_\odot$. The 1000 s timescale for variability observed in Ton S180 indicates that neither thermal nor viscous/radial drift phenomena can be held responsible for the observed fast variability. The values of these parameters are consistent with what is generally found for other Seyfert 1s. Haardt, Maraschi, & Ghisellini (1994) discuss a model where soft thermal photons from the accretion disk are Compton-upscattered in localized blobs of coronal plasma, constrained by magnetic loops from the disk. The resulting X-rays from the blobs then illuminate the disk and produce the so-called Compton Hump and Fe Kα emission line. The amplitudes and timescales of the rapid variations observed in Ton S180 are consistent with those expected as a result of stochastic noise in the number of reprocessing blobs, which depend on the formation and reconnection of magnetic loops.

The continuum fit to the mean spectrum yields a photon index $\Gamma = 2.44 \pm 0.02$. Our time-selected spectral fits give $\langle \Gamma \rangle = 2.47 \pm 0.07$ (1-σ error) with variations from 2.38 to 2.62. The steep index and the range ($\Delta\Gamma = 0.24$) are comparable with that observed in Akn 564 ($\Gamma = 2.54$, $\Delta\Gamma = 0.27$, Turner et al. 2001b), though the variations on a ~ 1 day timescale are significant in the case of Akn 564 and not for Ton S180 (where we detect variations of Γ in ~ 1 week timescale). The range of indices is also consistent with that found for the BLS1 NGC 7469 ($\Delta\Gamma = 0.32$, Nandra et al. 2000). This may indicate a fundamental similarity in the process which causes slope fluctuations, over a range of different AGN.

We confirm the presence of the soft X-ray emission component at energies < 2 keV previously observed by Fink et al. (1997), Comastri et al. (1998), and Turner, George, & Nandra (1998). This component rises above the power-law continuum $\lesssim 2$ keV, and has recently been shown to be a smooth continuum component rather than a blend of features, not only in Ton S180 (Turner et al. 2001a), but also in the NLS1 NGC 4051 (Collinge et al. 2001). Therefore, our time-selected spectroscopic analysis is particularly well suited to study its variability properties in particular and understand the nature of the soft hump in NLS1s in general. The soft hump shows flux variations on timescales as short as ~ 1 day (the shortest timescales our time-selected spectroscopy can study), ranging by a factor of 2.3 in flux over the observation, but always being present. We note that the fast variability observed in the soft hump of Ton S180 rules out an origin of the soft emission in large-scale components, such as circumnuclear starburst (as also concluded for the soft hump in Akn 564, Turner et al. 2001b). The hard flux, when similarly binned on timescales of a day, has a range of a factor 1.65. The softness ratio shows spectral variability on timescales as short as ~ 1000 s. In Ton S180 such fast spectral variability can be at-

tributed either to rapid changes in photon index or in the relative strengths of the soft hump and power-law. In addition to this evidence for divergent behavior on very short timescales, the soft hump and power-law show different trends on timescales of ∼ 1 week. The higher value of F_{var} measured in the soft than in the hard band is probably due to the combined effects of a larger amplitude of variation of the soft hump over the baselines of the observation, and the changes in spectral slope (which could preferentially affect the soft band if the pivot point lies within the hard band). The correlation observed between the soft hump flux and the photon index in Ton S180 is expected in disk-corona models where an increase of the flux in the soft X-ray/UV component can cool the corona and steepen the power-law continuum (Haardt, Maraschi, & Ghisellini 1994; Pounds, Done, & Osborne 1995). This is not the case for Akn 564, where Turner et al. (2001b) suggest the corona cooling might be saturated.

Iron Kα line emission is detected, with a broad, asymmetric profile. It is best parameterized by two Gaussian components; the narrow component peaks at $E_N = 6.81$ keV, which is consistent with emission from highly ionized gas, the broad component consistent with emission from either neutral or ionized gas. We caution about the reliability of this result because the signal-to-noise in this range is low and the errors on the fitted parameters are correspondingly large (Table 4.1). Therefore it seems that the best parametrization for the Fe Kα line is a broad ionized line, which is consistent with previous *BeppoSAX* (Comastri et al. 1998) and *ASCA* (Turner, George, & Nandra 1998) observations. The broad component is generally thought to originate in the innermost regions of the accretion disk around the central black hole (e.g., Fabian et al. 2000, and references therein), and so it is due to highly ionized Fe, while the narrow component is thought to be generated in the putative obscuring torus that extends on a parsec scale (Ghisellini, Haardt, & Matt 1994; Krolik, Madau, & Życki 1994; Yaqoob et al. 2001), and so is believed to be due to neutral material. In this context, the result of an ionized narrow Fe Kα component is therefore somewhat suprising. Note, however, that observations of such a feature are not unprecedented: Sako et al. (2000) and Ogle et al. (2000) detected narrow lines due to highly ionized iron in *Chandra* observations of Mkn 3 and NGC 4151, respectively.

The Fe Kα emission line has a very large equivalent width, EW ≈ 500 eV, as previously observed in other *ASCA* and *BeppoSAX* observations of Ton S180, Akn 564, and other NLS1s (Turner, George, & Nandra 1998; Comastri et al. 1998; Turner et al. 2001b). These EWs are interesting compared to a sample taken across the Seyfert 1 population (Nandra et al. 1997b), which found an average EW = 230 eV. One interpretation is in terms of an extreme Fe abundance in NLS1s, as proposed by Turner, George, & Netzer (1999) for Akn 564; this may, in turn, support the proposition that NLS1s are Seyfert galaxies in an early stage of evolution (Mathur 2000). Alternatively, Matt, Fabian, & Ross (1996) show that the expected EWs for predominantly H- and He-like Fe can be a factor of a few higher than those from neutral Fe. We do not detect significant variations of the Fe Kα line, on timescales of ∼ 1 day or of ∼ 1 week. We note that given our signal-to-noise in the Kα energy range for the 14 time-selected spectra, the line flux would have had to varied by at least a factor 2 for us to have detected the variation at > 99 % confidence level.

REFERENCES

Ballantyne, D. R., Iwasawa, K., & Fabian, A. C. 2001, MNRAS, 323, 506
Boller, Th., Brandt, W. N., & Fink, H. 1996, A&A, 305, 53
Boroson, T. A. & Green, R. F. 1992, ApJS, 80, 109
Brandt, W. N., Mathur, S., & Elvis, M. 1997, MNRAS, 285, L25
Brandt, W. N., Boller, T., Fabian, A. C., & Ruszkowski, M. 1999, MNRAS, 303, L53
Burke, B. E., Mountain, R. W., Harrison, D. C., Bautz, M. W., Doty, J. P., Ricker, G. R., & Daniels, P. J. 1991, IEEE Trans. ED-38, 1069
Collinge, M. J., Brandt, W. N., Kaspi, S., Crenshaw, D. M., Elvis, M., Kraemer, S. B., Reynolds, C. S., Sambruna, R., & Wills, B. 2001, ApJ, in press (astro-ph/0104125)
Comastri, A., et al. 1998, A&A, 333, 31
Comastri, A., et al. 2001, A&A, 365, 400
de Vaucouleurs, G., de Vaucouleurs, A., Corwin, H. G., Buta, R. J., Paturel, G., & Fouque, P. 1991, S&T, 82, 621
Dickey, J. M., & Lockman, F. M. 1990, ARA&A, 28, 215
Edelson, R., et al. 2001, submitted
Fabian, A. C., Rees, M. J., Stella, L., & White, N. E. 1989, MNRAS, 238, 729
Fabian, A. C., Iwasawa, K., Reynolds, C. S., & Young, A. J. 2000, PASP, 112, 1145
Fink, H. H., Walter, R., Schartel, N., & Engels, D. 1997, A&A, 317, 25
Gaskell, C. M., & Sparke, L. S. 1986, ApJ, 305, 175
Gaskell, C. M., & Peterson, B. M. 1987, ApJS, 65, 1
Ghisellini, G., Haardt, F., & Matt, G. 1994, MNRAS, 267, 743
Goodrich, R. W. 1989, ApJ, 342, 234

Guainazzi, M., Piro, L., Capalbi, M., Parmar, A. N., Yamaguchi, M., & Matuoka, M. 1998, A&A, 339, 327
Guilbert, P. W., Fabian, A. C., & McCray, R. 1983, ApJ, 266, 466
Haardt, F., Maraschi, L., & Ghisellini, G. 1994, ApJ, 432, L95
Huchra, J. P., Vogeley, M. S., & Geller, M. J. 1999, ApJS, 121, 287
Kaspi, S., Smith, P. S., Netzer, H., Maoz, D., Jannuzi, B. T., & Giveon, U. 2000, ApJ, 533, 631
Krolik, J. H., Madau, P., & Życki, P. T. 1994, ApJ, 420, L57
Kuraszkiewicz, J., Wilkes, B. J., Brandt, W. N., & Vestergaard, M. 2000, ApJ, 542, 631
Laor, A., Fiore, F., Elvis, M., Wilkes, B. J., & McDowell, J. C. 1997, ApJ, 477, 93
Laor, A. 1991, ApJ, 376, 90
Leighly, K. M. 1999a, ApJS, 125, 297
Leighly, K. M. 1999b, ApJS, 125, 317
Mason, K. O., Puchnarewicz, E. M., & Jones, L. R. 1996, MNRAS, 283, L26
Mathur, S. 2000, MNRAS, 314, L17
Matt, G., Fabian, A. C., & Ross, R. R. 1993, MNRAS, 264, 839
Matt, G., Fabian, A. C., & Ross, R. R. 1996, MNRAS, 278, 1111
Nandra, K., George, I. M., Mushotzky, R. F., Turner, T. J., & Yaqoob, T. 1997a, ApJ, 476, 70
Nandra, K., George, I. M., Mushotzky, R. F., Turner, T. J., & Yaqoob, T. 1997b, ApJ, 477, 602
Nandra, K., Le, T., George, I. M., Edelson, R. A., Mushotzky, R. F., Peterson, B. M., & Turner, T. J. 2000, ApJ, 544, 734
Ogle, P. M., Marshall, H. L., Lee, J. C., & Canizares, C. R. 2000, ApJ, 545, L81

Ohashi, T., et al. 1996, PASJ, 48, 157

Osterbrock, D. E., & Pogge, R. W. 1985, ApJ, 297, 166

Peterson, B. M. 1993, PASP, 105, 207

Peterson, B. M., Wanders, I., Horne, K., Collier, S., Alexander, T., Kaspi, S., & Maoz, D. 1998, PASP, 110, 660

Peterson, B. M. et al. 2000, ApJ, 542, 161

Pounds, K. A., Done, C., & Osborne, J. P. 1995, MNRAS, 277, L5

Sako, M., Kahn, S. M., Paerels, F., & Liedahl, D. A. 2000, ApJ, 543, L115

Stark, A. A., Gammie, C. F., Wilson, R. W., Bally, J., Linke, R. A., Heiles, C., & Hurwitz, M. 1992, ApJS, 79, 77

Turner, T. J., George, I. M., & Nandra, K. 1998, ApJ, 508, 648

Turner, T. J., George, I. M., & Netzer, H. 1999, ApJ, 526, 52

Turner, T. J., et al. 1999, in Proceedings of the 19th Texas Symposium on Relativistic Astrophysics and Cosmology, ed. J. Paul, T. Montmerle, & E. Aubourg (Saclay: CEA), E441

Turner, T. J., et al. 2001a, ApJ, 548, L13

Turner, T. J., Romano, P., George, I. M., Edelson, R., Collier, S. J., Mathur, S., & Peterson, B. M. 2001b, ApJ, in press (astro-ph/0105238)

Turner, T. J., et al. 2001c, in preparation

Vaughan, S., Pounds, K. A., Reeves, J., Warwick, R., & Edelson, R. 1999, MNRAS, 308, L34

Vaughan, S., Reeves, J., Warwick, R., & Edelson, R. 1999, MNRAS, 309, 113

Wandel, A., & Boller, Th. 1998, A&A, 331, 884

White, R. J., & Peterson, B. M. 1994, PASP, 106, 879

Wisotzki, A., Dreizler, S., Engels, D., Fink, H. H., & Heber, U. 1995, A&A, 297, L55

Yaqoob, T., et al. 2000, *ASCA* GOF Calibration Memo, ASCA-CAL-00-06-01, v1.0

Yaqoob, T., George, I. M., Nandra, K., Turner, T. J., Serlemitsos, P. J., & Mushotzky, R. F. 2001, ApJ, 546, 759

TABLE 2

COMPARISON OF THE PROPERTIES OF TON S180 AND AKN 564.

(1)	Ton S180[a] (2)	Akn 564[a] (3)	References[b] (4)	(5)
z	0.06198	0.0247	1	2
Galactic N_H (cm^{-2})	1.52×10^{20}	6.4×10^{20}	3	4
V (mag)	14.4	14.6	5	6
L_{2-10} (10^{43} ergs s^{-1})	4.9	2.4	7(3)	8(3)
R_{max} soft band	3.5	16	7(3)	8(3)
R_{max} hard band	3.9	14	7(3)	8(3)
R_{max} Soft Hump	2.33 ± 0.45	6.44 ± 3.30	7(5.3)	8(5.3)
R_{max} 2–10 keV	1.65 ± 0.02	3.97 ± 0.06	7(5.3)	8(5.3)
F_{var} (12 d, soft) (%)	19.12 ± 0.58	35.81 ± 0.81	7(3.1)	7
F_{var} (12 d, hard) (%)	17.26 ± 0.65	35.73 ± 0.70	7(3.1)	7
F_{var} (1 d, soft) (%)	variable	variable	7(3.1)	8(3.1)
correlates with X-ray	no	no	7(3.1)	8(3.1,7)
F_{var} (1 d, hard) (%)	variable, $<$ soft	variable, $<$ soft	7(3.1)	8(3.1)
correlates with X-ray	no	no	7(3.1)	8(3.1,7)
ICCF r_{max} (soft–hard band)	0.748	0.942	7(3)	8(7)
ICCF τ_{cent} (95% limit, d)[c]	< 0.07	< 0.02	7(3)	8(7)
Γ (Mean Spectrum)	2.44 ± 0.02	2.538 ± 0.005	7(4)	8(4)
$\Gamma_{min} - \Gamma_{max}$	2.38–2.62	2.45–2.72	7(5.2)	8(5.2)
$\Delta\Gamma$	0.24	0.27	7(5.2)	8(5.2)
PL soft band contribution (%)	72	75	7(4.1)	8(3.1)
Soft Hump Gaussian Fits: E (keV)	0.17 ± 0.17	0.57 ± 0.2	7(4.1)	8(4.1)
FWHM (keV)	$1.01^{+0.05}_{-0.12}$	0.36 ± 0.01	7	8
n (10^{-2} ph s^{-1} cm^{-2})	$1.50^{+0.37}_{-0.61}$	$1.25^{+0.12}_{-0.17}$	7	8
EW (eV)	94^{+23}_{-38}	110^{+11}_{-15}	7	8
Kα diskline Fits: E (keV)[d]	$6.40^{+0.27}_{-0.00p}$	$7.00^{+0.00}_{-0.13}$	7(4.2)	8(4.2)
EW (eV)	461^{+120}_{-84}	351 ± 85	7	8
i (deg)	35^{+22}_{-35p}	26 ± 2	7	8
Kα laor Fits: E (keV)[e]	$6.55^{+0.16}_{-0.15p}$	$6.99^{+0.01p}_{-0.13}$	7(4.2)	8(4.2)
EW (eV)	517^{+123}_{-111}	653 ± 85	7	8
i (deg)	23^{+14}_{-23p}	17^{+11}_{-17}	7	8

[a] 90 % confidence level uncertainties.

[b] The numbers in parenthesis refer to the sections where the relevant information is found in the given references.

[c] Lag of hard relative to soft flux.

[d] Best parametrization for Ton S180 is by two Gaussians with peak energy $E_N = 6.81^{+0.08}_{-0.12}$ keV and $E_B = 6.58^{+0.25}_{-0.28}$ keV.

[e] Best-fit model for Akn 564 (Turner et al. 2001b).

References. — 1: Wisotzki et al. (1995); 2: Huchra, Vogeley & Geller (1999); 3: Stark et al. (1992); 4: Dickey & Lockman (1990); 5: NED; 6: de Vaucouleurs et al. (1991); 7: This work; 8: Turner et al. (2001b).